Displacive radiation effects in the monazite- and zircon-structure orthophosphates

A. Meldrum*
Department of Earth and Planetary Sciences, University of New Mexico, Albuquerque, New Mexico 87131-1116

L. A. Boatner
Oak Ridge National Laboratory, Oak Ridge, Tennesee 37831-6056

R. C. Ewing†
Department of Earth and Planetary Sciences, University of New Mexico, Albuquerque, New Mexico 87131-1116

(Received 22 May 1997)

Monazite-structure orthophosphates, including $LaPO_4$, $PrPO_4$, $NdPO_4$, $SmPO_4$, $EuPO_4$, $GdPO_4$, and natural monazite, and their zircon-structure analogs, including $ScPO_4$, YPO_4, $TbPO_4$, $TmPO_4$, $YbPO_4$, and $LuPO_4$, were irradiated by 800 keV Kr^{2+} ions in the temperature range of 20 to 600 K. The critical amorphization dose was determined *in situ* as a function of temperature using selected-area electron diffraction. Amorphization doses were in the range of 10^{14} to 10^{16} ions/cm^2, depending on the temperature. Materials with the zircon structure were amorphized at higher temperatures than those with the monazite structure. The critical amorphization temperature ranged from 350 to 485 K for orthophosphates with the monazite structure and from 480 to 580 K for those with the zircon structure. However, natural zircon ($ZrSiO_4$) can be amorphized at over 1000 K. Within each structure type, the critical temperature of amorphization increased with the atomic number of the lanthanide cation. Structural topology models are consistent with the observed differences between the two structure types, but do not predict the relative amorphization doses for different compositions. The ratio of electronic-to-nuclear stopping correlates well with the observed sequence of susceptibility to amorphization within each structure type, consistent with previous results that electronic-energy losses enhance defect recombination in the orthophosphates. [S0163-1829(97)04545-1]

I. INTRODUCTION

Orthophosphates are materials that are composed of isolated PO_4 tetrahedra, analogous to ''orthosilicates.'' The most common naturally occurring orthophosphates are apatite [$Ca_5(PO_4)_3$(F,Cl,OH)] and monazite ($LnPO_4$), where Ln refers to lanthanide elements, usually La and Ce. In natural monazite, however, the entire lanthanide series may be found in decreasing abundance with increasing atomic number.[1] The orthophosphate mineral xenotime (YPO_4) is a relatively common accessory mineral in plutonic and metamorphic rocks and has a crystal structure related to that of the $LnPO_4$ compounds.[2–4] Naturally occurring monazite was used in this study, as well as synthetic single crystals of $LaPO_4$, $PrPO_4$, $NdPO_4$, $SmPO_4$, $EuPO_4$, $GdPO_4$, $TbPO_4$, $TmPO_4$, $YbPO_4$, $LuPO_4$, and the nonlanthanide phases $ScPO_4$ and YPO_4.

The lanthanide orthophosphates (plus $ScPO_4$ and YPO_4) are part of the larger ABO_4 mineral group, which includes the silicates: zircon ($ZrSiO_4$), thorite (tetragonal $ThSiO_4$), huttonite (monoclinic $ThSiO_4$), and nonhydrated coffinite ($USiO_4$). Depending on the radius of the A-site cation, the ABO_4 minerals crystallize in either the monazite or zircon structure type, named after the natural minerals. For the $LnPO_4$ compounds, if the radius of the A-site cation is less than that of Gd (covalent radius = 1.247 Å),[5] the material will have the tetragonal ($I4_1/amd$, $Z=4$) zircon structure. This structure includes $ScPO_4$ and YPO_4, in addition to $TbPO_4$, $TmPO_4$, $YbPO_4$, and $LuPO_4$.[2,3,4,6] All other orthophosphates in the present study have the lower-symmetry monoclinic ($P2_1/n$, $Z=4$) monazite structure.[2,6–8] If the size of the A-site cation is near the crossover radius (e.g., Gd and Tb), then the monazite structure is the low-temperature form, and the zircon structure is the high-temperature form.[9] There is also a low-temperature hexagonal structure that has rarely been observed because of its low irreversible transition temperature of approximately 800 K.[10]

The monazite and zircon structure types are closely related. The zircon structure can be viewed as being composed of alternating edge-sharing AO_8 polyhedra and BO_4 tetrahedra forming chains parallel to the c axis (Fig. 1). In the monazite structure, a ninth oxygen is introduced into the coordination sphere of the larger A-site cation. The oversized cation causes structural distortions, involving a rotation of the tetrahedra and a lateral shift of the (100) plane by 0.22 nm along [010],[2] thereby reducing the symmetry from $I4_1/amd$ to $P2_1/n$ (i.e., the monazite structure: Fig. 1). The two structures are, therefore, closely related, and the monazite structure can be viewed as a low-symmetry derivative of the zircon structure.

The effects of displacive irradiation on various ceramic materials have been extensively investigated, stimulated in part by applications of ceramics in the nuclear industry, including their proposed use as ''radiation-resistant'' reactor materials[11–13] or as single-phase or multiphase crystalline nuclear waste forms. In particular, zircon is a suggested host phase for excess weapons plutonium,[14–16] and monazite is a suggested waste form for high-level nuclear waste.[9,17,18] $LaPO_4$ is also currently under active investigation in Japan for the precipitation of actinides from nuclear waste tanks.[19]

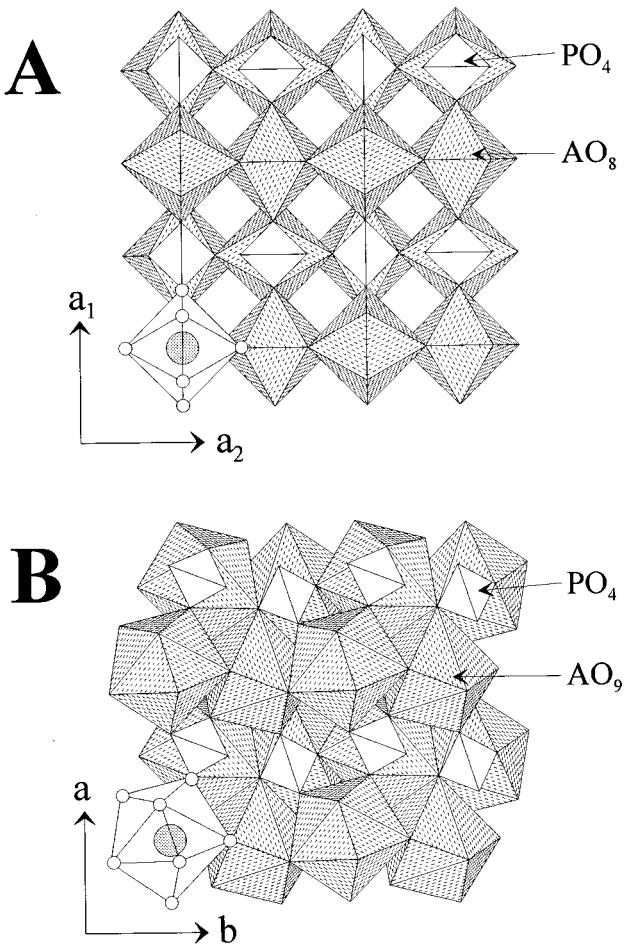

FIG. 1. Polyhedral diagrams showing the zircon and monazite structure types, generated using the data in Refs. 4 and 7. In the zircon structure (a), the smaller *A*-site cations (shaded circle, bottom-left corner of each diagram) are coordinated to eight oxygens (open circles) and the PO_4 tetrahedra are not distorted (equal P-O bond lengths). The presence of the larger *A*-site cations distorts the zircon structure by rotating, distorting, and shifting the PO_4 tetrahedra and this introduces a ninth oxygen into the coordination sphere of the lanthanide cation, producing the monazite structure type (b).

Additional motivation is derived from the often unique optoelectronic properties of amorphous or implanted ceramic phases [e.g., Refs. 20 and 21]. Specifically, ion-beam-amorphized zircon is a potential optical waveguide material,[22] and amorphous orthophosphates may also have applications in electron lithography.[23,24]

Natural monazite is almost invariably crystalline despite containing greater than 10 wt. % UO_2+ThO_2 on average. Natural zircon, while typically containing less than 5000 ppm uranium, is often amorphous (metamict).[25] Because of the natural occurrence of U and Th in these minerals, they are widely used in geochronology, however, radiation effects can disturb the U-Pb systematics (e.g., see Refs. 25 and 26). Low-temperature lead loss in the outer layers of zircon crystals is frequently observed and can lead to incorrect ages.[27] This may be related to enhanced leaching of radiogenic daughter products due to radiation damage, and recent work has indicated that the reliability of U-Pb zircon ages may be directly related to U-content through radiation damage processes.[28] Monazite, on the other hand, does not suffer lead loss, possibly related to rapid natural annealing of α-recoil tracks.[29–31]

The lanthanide orthophosphate series [including $ScPO_4$, YPO_4, and the silicate zircon ($ZrSiO_4$)] offers an excellent opportunity to evaluate the models used to predict the susceptibility of ceramics to irradiation-induced amorphization. The regular structural and chemical variations in the ABO_4 phases allow a systematic investigation of the competing effects of structure and chemistry on the amorphization process. In the present study, we present results for the $LnPO_4$ compounds and natural monazite, representing an overall variation from $Z=21$ to $Z=71$ for the *A*-site cation. These results are compared to previous data for zircon,[32–34] and the effects of chemical impurities are also investigated.

II. EXPERIMENT

A. Sample preparation

Single crystals of the orthophosphates were grown by the flux method.[9] The pure lanthanide oxides (Ln_2O_3) were combined with lead hydrogen phosphate and heated to $\sim$1630 K in a platinum crucible. The system was held at this temperature for several days, cooled at 1 K per hour to 1170 K, and then rapidly cooled to room temperature. Single orthophosphate crystals were then removed from the $Pb_2P_2O_7$ flux by boiling in nitric acid for several weeks. The composition was subsequently verified by energy dispersive spectroscopy (EDS), and x-ray-diffraction analysis confirmed the monazite and zircon structure types. Natural monazite from Ontario, Canada was also used in these experiments in order to determine the effects of chemical impurities on the irradiation results.

Prior to irradiation, the composition of the natural samples was determined using a JEOL733 electron microprobe. The microprobe was operated at an accelerating voltage of 15 keV, and the beam current was 20 nA. The beam diameter was approximately 1 μm. All elements, including oxygen, were determined by wavelength-dispersive spectrometry (WDS) using lanthanide orthophosphate standards. Data were reduced by the ZAF-4 correction technique using Oxford GENIE microprobe automation and data analysis software. The H_2O content was determined by loss-on-ignition (LOI) at 1300 K.

The samples were sectioned parallel to the *c* axis, except for the natural monazite samples, which were sectioned randomly because of the absence of well-formed crystal faces to indicate the crystallographic orientation. The samples were glued to copper TEM foils and hand polished to a thickness of approximately 10 μm. They were then ion milled to perforation at room temperature using 4 keV Ar ions at an incident angle of 20° to the sample surface. The beam energy was lowered to 3 keV, and the samples were irradiated for ten minutes subsequent to perforation. Prior to ion-irradiation, the samples were carbon coated and examined in a JEOL2000FX electron microscope to ensure that the materials were not altered by the ion-milling process and that the natural samples contained no observable radiation damage.

TABLE I. Composition of the natural monazite used in this study.

Element	wt. %	Element	wt. %
La	10.4	Ca	0.62
Ce	23.9	Fe	0.17
Pr	2.5	Y	0.95
Nd	11.1	P	11.1
Sm	1.6	Al	0.05
Pb	0.24	B	<0.4
Th	8.3	Si	0.52
U	0.6	LOI	0.89
O	22.8	Total	95.74

B. Ion irradiation

The materials were irradiated using the IVEM Facility at Argonne National Laboratory. This facility consists of a Hitachi H9000NAR intermediate-voltage electron microscope interfaced to a 400 keV ion accelerator. Irradiations were done at 10° off the [001] zone axis to avoid channeling effects. 800 keV Kr^{2+} ions were chosen in order to compare the present results to earlier work using Kr and because of the minimal chemical effects of an implanted noble gas. Irradiations were performed over the temperature range 20 to 600 K using a liquid-helium cooling stage or a single-tilt hot stage. The ion flux was 1.25×10^{12} ions cm^{-2} s^{-1}. Amorphization was observed *in situ* by the loss of electron-diffraction maxima. During irradiation, the electron beam was turned off to minimize the combined effects of electron and ion irradiation. Subsequent high-resolution TEM was done using a JEOL2010 electron microscope. TRIM-96 calculations[35] were used to model the ion ranges and target displacements.

III. RESULTS

A. Electron microprobe analysis

The results of the electron microprobe analyses for the natural monazite are given in Table I. The impurity content in the monazite is typically high (e.g., >10 wt. % ThO_2). The analytical totals were low (~96 wt. %), indicating the possible presence of impurity elements which were not analyzed, however, the results give a near-perfect stoichiometry of $A_{1.17}B_{1.05}O_4$. Approximately 1 wt. % of the mineral was volatilized by LOI, presumably due to the loss of structural water (i.e., the mineral rhabdophane is simply hydrated monazite). Because impurities in these samples are needed in order to determine their effect on the ion-irradiation results, these samples were deemed suitable for irradiation.

B. Ion irradiations

Radiation-induced amorphization by 800 keV Kr^{2+} ions occurred in all the materials investigated. At low doses, amorphization associated with individual displacement cascades was observed (Fig. 2). As the dose was increased, these domains, having image contrast which can be interpreted as that of amorphous material, increased in size and overlapped leaving a few slightly rotated crystalline islands which eventually disappeared as the material became fully amorphous. The critical amorphization dose (D_c) is the lowest dose at which there are no observable electron-diffraction maxima, and the diffraction pattern contained only amorphous rings. In actuality, the material may or may not be fully amorphized even when the diffraction maxima have entirely disappeared,[36] however, as long as this criterion is used consistently, valid comparisons can be made (with the reasonable assumption that the image transfer functions are similar for these materials). The critical amorphization dose was found to be up to several times higher in the presence of

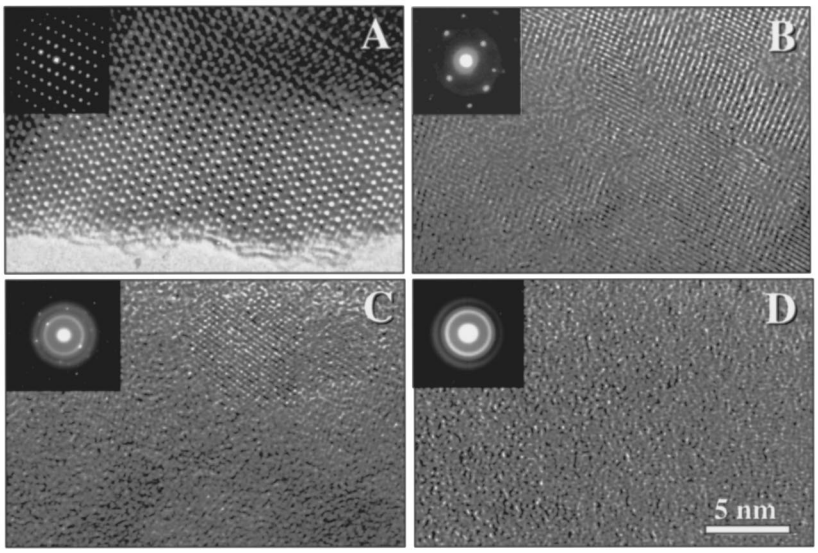

FIG. 2. High-resolution TEM images and corresponding electron-diffraction patterns showing an amorphization sequence in natural monazite (Ref. 44): unirradiated (a), 8.55×10^{13} ions/cm^2 (b), 1.71×10^{14} ions/cm^2 (c), 2.56×10^{14} ions/cm^2 (d). All samples were irradiated at 310 K. Similar sequences could not be obtained for the pure orthophosphates because of the rapidity of electron-irradiation-induced crystallization in the TEM.

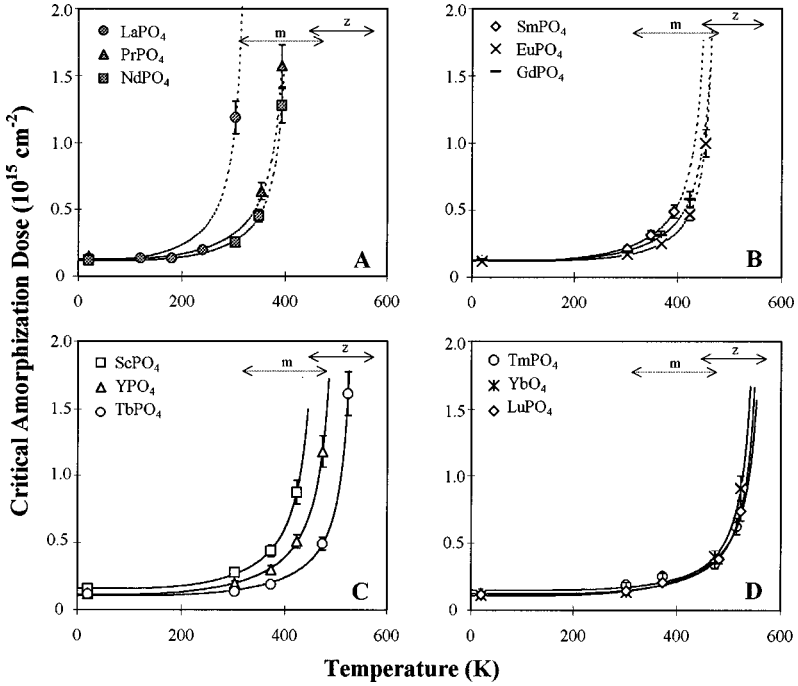

FIG. 3. Critical amorphization dose as a function of temperature for the orthophosphates. The data was separated into four panels for clarity; (a) and (b) show the data for the monazite-structure orthophosphates, and (c) and (d) for those having the zircon structure. The lines through the points were plotted using a least-squares refinement of Eq. (2) (see text). The error bars represent $\pm 10\%$. The arrow marked with an *m* in the top left of each graph highlights the range of T_c values for the monazite structure and that with a *z* those for the zircon structure.

the electron beam in the TEM, so all irradiations were done with the electron beam turned off. The effect of increasing temperature was found to cause an exponential increase in D_c (Fig. 3), as documented for many other ceramic materials.[13,34,37]

The critical amorphization dose at room temperature for the different materials was difficult to distinguish within experimental error, so T_c (the temperature above which amorphization was not induced) was used to compare the kinetics of amorphization. Irradiations at temperatures higher than T_c were performed to ensure that the values estimated from the curves were correct. At $T > T_c$, only incomplete amorphization could be induced at a dose of 1.5 to 2.0 $\times 10^{15}$ ions/cm^2, and at $T > 100 + T_c$, the ion beam was observed to induce crystallization in some previously amorphized samples.

The effect of the chemical variation is evident in Fig. 3. Within the orthophosphates, T_c was found to vary consistently with the atomic number of the *A*-site cation within each structure type. In general, the effect of increasing *Z* was to cause an increase in T_c. However, some irregularities were observed. For example, $EuPO_4$ was slightly easier to amorphize at elevated temperatures than $GdPO_4$, and $LaPO_4$ has a remarkably low T_c, such that the difference between $LaPO_4$ and $PrPO_4$ is larger than that between $PrPO_4$ and $GdPO_4$.

Materials having the zircon structure can be amorphized at higher temperatures than those having the monazite structure. The critical temperatures for the monazite-structure materials [Figs. 3(a) and 3(b)] are lower than for the zircon-structure materials [Figs. 3(c) and 3(d)], although some overlap occurs because of the atomic-number effect, described above. The observed difference between $GdPO_4$ (monazite structure) and $TbPO_4$ (zircon structure) illustrates the structural dependence of the critical amorphization temperature. Gd and Tb are adjacent on the periodic table, but the critical amorphization temperature for $TbPO_4$ is 545 K, as compared to 485 K for $GdPO_4$. The structural effect can counterbalance the chemical effect so that the results for $ScPO_4$ are similar to those for $GdPO_4$ despite the large difference in the atomic number of the *A*-site cation.

In general, the phosphates are more difficult to amorphize (or are correspondingly more easily annealed during irradiation) than their isostructural silicate analogs. This effect is

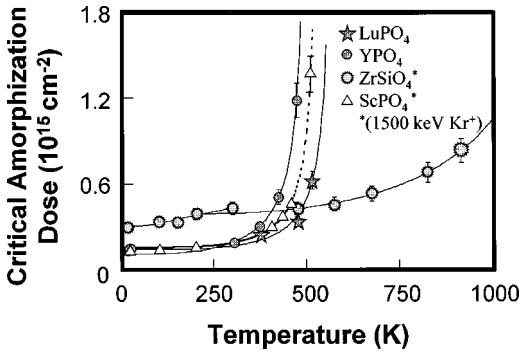

FIG. 4. Comparison of the results for YPO_4 and $LuPO_4$ (800 keV) and $ScPO_4$ (1500 keV) from the present study, with those for zircon (1500 keV).[34] The lines are plotted as in Fig. 3, and the error bars are $\pm 10\%$. Zircon was observed to undergo two stages of irradiation-enhanced annealing. Despite the structural and chemical similarities, the orthophosphates have much lower critical amorphization temperatures than the orthosilicate zircon.

TABLE II. Critical amorphization dose at 0 K (D_0), irradiation-enhanced activation energies for annealing (E_a), and critical temperatures of amorphization (T_c) for 800 keV Kr^{2+} irradiation of the suite of orthophosphates. The values are calculated from a least-squares refinement of Eq. (2), and the dpa values are calculated using Eq. (1).

Compound	D_0 [cm^{-2} ($\times 10^{14}$)]	D_0 dpa	E_a (eV)	T_c (K)
	monazite structure			
$LaPO_4$	1.23	0.35	0.032	333
$PrPO_4$	1.26	0.38	0.046	419
$NdPO_4$	1.16	0.35	0.054	418
$SmPO_4$	1.21	0.38	0.057	472
$EuPO_4$	1.22	0.39	0.093	479
$GdPO_4$	1.24	0.39	0.069	485
monazite	1.02	0.31	0.078	450
	zircon structure			
$ScPO_4$	1.56	0.37	0.064	477
YPO_4	1.12	0.31	0.054	512
$TbPO_4$	1.04	0.37	0.074	545
$TmPO_4$	1.07	0.31	0.079	563
$YbPO_4$	1.21	0.39	0.099	570
$LuPO_4$	1.48	0.48	0.113	577

quite pronounced, as shown by a comparison of results for YPO_4 and $LuPO_4$ to $ZrSiO_4$ (Ref. 34) (Fig. 4). The molar mass and density of YPO_4 and $ZrSiO_4$ are nearly identical (184 vs 187 g/mol and 4.26 vs 4.65 g/cm^3, respectively). They have the same crystal structure, but show a very different temperature dependence of the critical amorphization dose. The critical temperature for zircon is about 600 K higher than for YPO_4 and $LuPO_4$ (the most easily amorphized of the orthophosphates), despite the similarities in structure, density, and molar mass.

A potential caveat is that the zircon was irradiated by 1500 keV Kr^+ ions,[34] compared to 800 keV Kr^{2+} for the present experiments. However, Abe *et al.*[37] demonstrated that T_c increases with decreasing ion energy for graphite, presumably due to the greater cross section for nuclear interactions as the low-energy ions pass through the TEM foil. Thus the observed differences in T_c would be expected to be a minimum. Nonetheless, the results for 1500 keV Kr^+ irradiation of $ScPO_4$ (molar mass: 140 g/mole, density: 3.71 g/cm^3) are also shown in Fig. 4, and the difference in T_c is similarly large.

TRIM-96 calculations (full cascades) were used to model the results and to calculate the displacements per atom (dpa) in the target:

$$D_c(\text{dpa}) = \frac{C_t f(\text{ions/cm}^2)}{n}, \tag{1}$$

where f is the critical amorphization fluence, C_t is the number of displacements per ion per unit depth calculated by TRIM-96, and n is the atomic density. The displacement energy was estimated to be 20 eV and the binding energy to be 2 eV for the purpose of these calculations. The results calculated in this way for D_0 are given in Table II. Ion-range calculations show that the amount of implanted Kr is less than 1 at. % for the 800 keV irradiations, assuming a thickness of 200 nm.

IV. DISCUSSION

Previous work on irradiation effects in the orthophosphates is quite limited. Karioris *et al.*[38] irradiated monazite and several related phases with 3 MeV Kr^+ ions at ambient temperature. They found that monazite amorphizes at a dose of less than 5 ions/nm^2, as compared to over 2000 ions/nm^2 for ThO_2, for example, and concluded that monazite is not resistant to radiation damage. However, the monazite was fully annealed after heating for 20 h at 570 K. In contrast, the isostructural silicate huttonite ($ThSiO_4$) began to recrystallize at approximately 1050 K. In another study, Karioris *et al.*[39] completed irradiations on a variety of minerals, including monazite, zircon, and huttonite. The measured damage cross sections (0.56 nm^2 for monazite compared to 0.33 nm^2 for zircon, for example) showed that monazite is relatively easily amorphized at room temperature. Robinson[40] simulated Ar-ion irradiation of monazite using the binary collision approximation computer code MARLOWE. Amorphization was suggested to occur when collision cascades begin to overlap, similar to zircon which may require a double overlap to trigger amorphization.[34]

A. Determination of activation energies for irradiation-enhanced annealing

The shape of the curves of the critical amorphization dose versus temperature plots shown in Fig. 3 can be considered in the context of a variety of models. For example, Abe *et al.*[37] interpreted similar curves for graphite to be attributable to two stages of defect recombination during irradiation (not related to the two stages in zircon[34]), the first of which accounts for the relatively flat part of the curve and the second the steep portion. Conversely, the entire curve can be modeled by a single equation: the most commonly used model was proposed by Weber *et al.*[34] and Weber and Wang,[41] and is partly based on an earlier ''thermal-spike'' model by Morehead and Crowder.[42] According to the latter model, amorphization occurs directly within cylindrical damage cascades of radius r. The effect of temperature is to increase Δr, the radius of material that recrystallizes epitaxially at the edge of the cascade during the post-quench annealing stage. Weber's model[34,41] does not assume cylindrical cascades or direct-impact amorphization. The critical amorphization dose is then related to temperature through a dynamic irradiation-enhanced, diffusion-driven annealing activation energy E_a:

$$\ln(1 - D_0/D) = \ln(1/\phi\sigma\tau) - E_a/kT, \tag{2}$$

in which D_0 is the critical amorphization dose at 0 K (extrapolated), ϕ is the ion flux, σ is the amorphization or damage cross section, τ is a time constant, and k is Boltzmann's constant. Previously, activation energies were obtained by calculating the slope of a $\ln(1-D_0/D)$ vs $1/kT$ curve on an Arrhenius plot in which the value of D_0 was estimated by extrapolation. The critical amorphization temperature is then derived from Eq. (2):

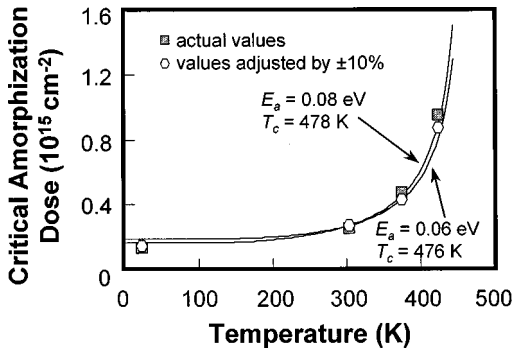

FIG. 5. Variations of E_a and T_c calculated by Eqs. (2) and (3) (see text) that can result from experimental error. The shaded squares represent the actual data values for $ScPO_4$ irradiated by 800 keV Kr^{2+}, and the E_a and T_c values are from Table II. A random variation of $\pm 10\%$ gives the curve marked by the open polygons. The E_a value was changed by approximately 25%, but the T_c value remained almost unchanged. Any error in the temperature measurements would similarly be strongly reflected in the values of E_a. Therefore, T_c is a more reliable annealing parameter than is E_a in these types of experiments.

$$T_c = E_a/[k \ln(1/\phi\sigma\tau)]. \quad (3)$$

This method has been applied to calculate values of E_a for a wide variety of materials (e.g., Refs. 13, 34, 43, 44). Two important points should be made concerning this model. First, ionization effects from the ion beam are not specifically calculated. Ionization effects may be negligible, as demonstrated for zircon,[32] although in other insulating ceramics they have been shown to contribute to damage accumulation[45] or, under certain conditions, to enhance defect recombination.[11,46,47] Second, the calculated activation energy is strongly dependent on the slope of the curve and, hence, on the value chosen for D_0. The activation energy is not dependent on T_c, rather, T_c is calculated by Eq. (3) through a rearrangement of Eq. (2). E_a thus depends only on the degree of curvature of the lines in Fig. 3.

Traditionally, the dose obtained at 20 K was taken to be D_0. Then, the slope of an Arrhenius plot of $\ln(1-D_0/D)$ vs $\ln(\phi\sigma\tau)$ provided the value for E_a. Alternatively, Meldrum *et al.*[43] showed that a least-squares refinement could be applied to Eq. (2) to solve simultaneously for E_a, D_0, and $\ln(1/\phi\sigma\tau)$, the advantage being that every point in the data set then contributes to the value taken for D_0. Activation-energy values can change by as much as 100% by this method, as compared to a simple extrapolation for D_0. Table II gives a list of activation-energy values calculated in this way for the orthophosphates.

The values obtained for E_a using Eq. (2) should be used cautiously. The calculated values are surprisingly low (usually less than one tenth of an electron volt). The activation energy for epitaxial thermal recrystallization of Si, for example, is 2.7 eV, which can be lowered to 0.62 eV under 1.5 MeV Xe irradiation.[48] The latter values were obtained by measuring the growth rate of crystallites during irradiation and are an order of magnitude higher than those typically obtained using the above model. Additionally, the 10% error bars in Fig. 3 can lead to a 50% or greater change in the calculated activation energy (Fig. 5), and this problem is further exacerbated if one were to consider errors in measuring the temperature. The relatively consistent increase in E_a with the atomic number of the *A*-site cation (Table II) suggests that these values can be used for comparative purposes, but their physical meaning is probably limited. The calculated values for T_c, however, are relatively insensitive to experimental error (Fig. 5) and can be directly confirmed experimentally.

$EuPO_4$ has an anomalously high E_a, reflecting the steeper curve in Fig. 3 (the curve for $EuPO_4$ actually crosses several other curves). The unusual behavior of $EuPO_4$ may be explained by the possibility of valence change during irradiation. If some of the Eu^{3+} is converted to Eu^{2+} then the material would be expected to be harder to anneal under irradiation because of charge-balance considerations. A similar effect is well known in the crystallization of lanthanide-bearing phases from a melt and is called the ''Eu anomaly'' (e.g., see Ref. 49). The Eu anomaly occurs because of the resistance of Eu^{2+} to crystallize into lanthanide-bearing minerals, resulting in exceptionally low Eu concentrations.

B. Effect of crystal structure

The effect of crystal structure in these experiments can be partially explained by using a structural-topology-based model such as that proposed by Hobbs.[50] According to this model, for any given material, the susceptibility to amorphization (at zero K) is governed by the connectivity of the cation polyhedra. Therefore, the only requirement for the application of this model is a knowledge of the corner, edge, and face sharing for all of the polyhedra. Materials that are structurally highly constrained (high topological connectivity for the cation polyhedra) are proposed to be resistant to radiation-induced amorphization. Thus, NaCl, for example, in which each anion represents a shared corner for six cation polyhedra, is more difficult to amorphize than SiO_2, in which each oxygen cross links only two SiO_4 tetrahedra.

Wang *et al.*[51] used Hobbs' model as a starting point to propose a semiempirical means of predicting the susceptibility to amorphization. In that work, it was proposed that materials that are good glass formers are relatively susceptible to amorphization. Wang's model attempts to account for the differences in bonding (e.g., bond length and bond valence) in otherwise identical structures, although several potentially risky assumptions must be made (e.g., the model may assume bonding that is not actually present).

Hobb's model appears to work well for relatively simple structures. For more complicated structures, Hobbs *et al.*[52] proposed that some polytopes may be weak links (e.g., SiO_4 tetrahedra in zircon) that control the response to displacive irradiation. Keeping in mind that this is a simplification, the average connectivity for the lanthanide polyhedra is 6 in the monazite structure type, as compared to 5.3 in the zircon structure type. All other factors being equal, a lower connectivity leads to easier amorphization, possibly consistent with the higher critical temperatures for materials having the zircon as compared to the monazite structure type. This analysis assumes no crossing of the temperature-dose lines (not valid for $EuPO_4$). However, the model gives identical results within each structure type, regardless of chemistry and is, therefore, unable to explain the large observed difference

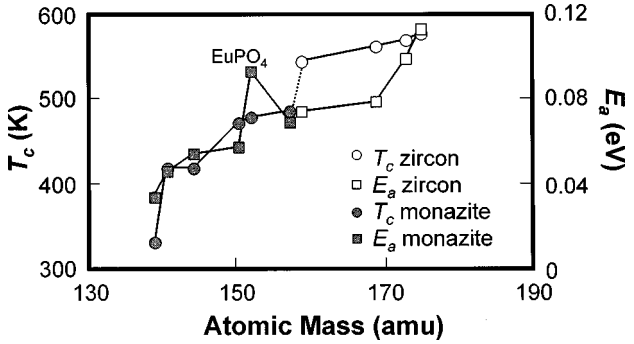

FIG. 6. T_c (circles) and E_a (squares) plotted as a function of atomic mass for the lanthanide orthophosphates with the monazite (filled symbols) and zircon (open symbols) structures. In general, both T_c and E_a increase with the mass of the A-site cation. $EuPO_4$ (labeled) has an anomalously high E_a, as discussed in the text. Notice the large increase in T_c between the monazite and zircon structure types (dashed line).

between, for example, $ScPO_4$ and $LuPO_4$ (or $ZrSiO_4$). Wang's model[51] is unable to correctly predict the differences within the zircon-structure compounds, although some success was obtained for those with the monazite structure.

C. Nuclear cross sections and energy transfer

Figure 6 shows the E_a and T_c values plotted as a function of the mass of the A-site cation. The trend of increasing E_a and T_c with atomic mass for both structure types is clear. In general, the phosphates with heavier cations require a lower dose for amorphization than those with lighter cations or, conversely, undergo less dynamic annealing. There is a pronounced jump in the T_c values between the monazite and zircon-structure types.

The general increase in the ''ease of amorphization'' with increasing mass of the A-site cation can be partially explained by an examination of nuclear cross sections. The cross sections for nuclear interactions with 800 keV Kr^{2+} ions were calculated after Ziegler *et al.*:[53]

$$\epsilon_n(E)=\frac{8.462Z_1Z_2S_n(E_r)}{(M_1+M_2)(Z_1^{0.23}+Z_2^{0.23})}\ \text{eV cm}^2/10^{15}\ \text{atoms}, \tag{4}$$

where M_1, M_2, Z_1, and Z_2 refer to the mass and atomic number of the ion and the target, respectively, and $S_n(E_r)$ is the reduced nuclear stopping power:

$$S_n(E_r)=\frac{\ln(1+1.1383E_r)}{2(E_r+0.01321E_r^{0.21226}+0.19593E_r^{0.5})} \tag{5}$$

for $E_r<30$ keV, as in these experiments. E_r, the reduced energy, is

$$E_r=\frac{32.53M_2E}{Z_1Z_2(M_1+M_2)(Z_1^{0.23}+Z_2^{0.23})}. \tag{6}$$

Bragg's linear additivity rule was applied to obtain the compound cross sections, using the mole fractions of the constituent elements of the compound. The nuclear stopping cross sections calculated in this manner increase with the atomic number of the A-site cation (Table III). However, the maximum energy transfer (E_t) by nuclear collisions, calculated using the following simple elastic-interaction model:

$$E_t=4M_1M_2E/(M_1+M_2)^2 \tag{7}$$

decreases as the mass of the A-site cation increases; thus offsetting the higher nuclear cross sections in terms of net deposited energy. Thus, nuclear stopping alone is probably not sufficient to explain the experimental results.

TABLE III. Comparison of nuclear cross sections, calculated according to Eqs. (4)–(6) (see text), maximum energy transfers by ballistic collisions [Eq. (7)], electronic and nuclear stopping powers calculated using TRIM-96, and electronic to nuclear stopping power ratio (ENSP). The dotted line divides materials having the monazite structure (above) and zircon structure (below), as in Table I.

Compound	σ_n (eV cm^2 per 10^{15} atoms)	E_t keV	dE/dx_e eV/A	dE/dx_n eV/A	ENSP
Monazite structure					
$LaPO_4$	1.93	187.75	128	127	1.008
$PrPO_4$	1.96	187.08	125	133	0.940
$NdPO_4$	1.96	185.95	107	115	0.930
$SmPO_4$	1.97	183.83	125	138	0.906
$EuPO_4$	1.98	183.28	123	140	0.879
$GdPO_4$	1.97	181.43	125	141	0.887
Zircon structure					
$ScPO_4$	1.63	177.86	128	130	0.985
YPO_4	1.82	199.82	118	128	0.922
$TbPO_4$	1.98	180.84	131	148	0.885
$TmPO_4$	2.00	177.31	111	132	0.841
$YbPO_4$	2.00	175.86	125	145	0.862
$LuPO_4$	2.00	175.17	124	147	0.844

D. Combined effects of electronic and nuclear energy loss

The present results can be interpreted through an analysis of the electronic and nuclear stopping powers and the distribution of energy loss in the target material. The overall nuclear and electronic energy losses dE/dx_n and dE/dx_e calculated by TRIM-96 for the different targets are presented in Table III. Density values calculated from the structural data given by Ni *et al.*[2] were used in obtaining these values. The values do not vary linearly as a function of the mass of the A-site cation due in part to the differences in density.

The effect of ionizing radiation in certain energy ranges appears to promote defect recombination in many ceramic oxides. Meldrum *et al.*[23,24] demonstrated that subthreshold electron-irradiation can induce crystallization as a result of ionization processes in amorphous orthophosphates. Zinkle[11,46,47] has shown that the rate of dislocation-loop formation is lower when the ratio of the electronic-to-nuclear stopping power (ENSP) is high, for example, in spinel ($MgAl_2O_4$), α-alumina (Al_2O_3), and MgO. The ENSP ratios are given in Table III and are plotted against T_c and E_a in Fig. 7. The critical amorphization temperature decreases uniformly as a function of ENSP. This is consistent with the hypothesis that when the ENSP ratio is high, the rate of defect accumulation is low (due to enhanced point defect mobilities). The trends for the monazite and zircon structure

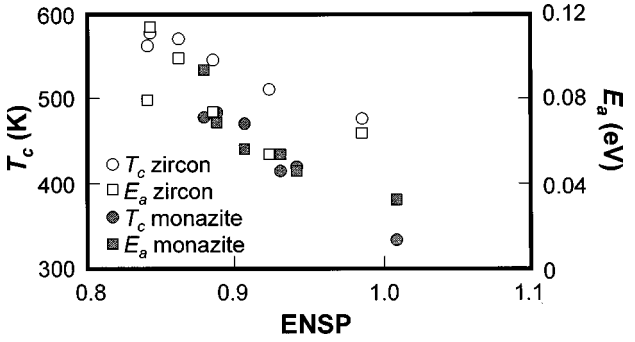

FIG. 7. T_c and E_a plotted as a function of the ratio of electronic-to-nuclear stopping powers (ENSP). Symbols are the same as in the previous figures. The activation energies and critical temperatures decrease with increasing ENSP, consistent with previous results for spinel and α-alumina (Refs. 11, 46, and 47) and for the electron irradiation of amorphous orthophosphates (Refs. 23 and 24), which showed that ionizing radiation can enhance defect recombination. Using T_c as the amorphization criterion, the data are divided into two lines of roughly equal slope, showing a high correlation with ENSP. For the same ENSP, the zircon-structure materials have higher values of T_c and E_a.

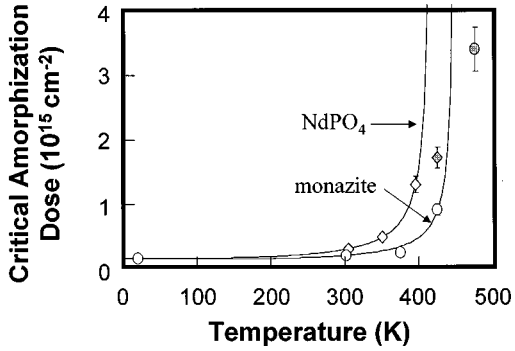

FIG. 8. Comparison of the amorphization curves for natural monazite and $NdPO_4$ (having a similar ''average'' mass of the A-site cation), demonstrating the effect of impurities on the temperature dependence of the critical amorphization dose. The effect of impurities in the natural samples is to increase the critical amorphization temperature, reflecting a greater resistance to crystallization. The filled symbols represent doses at which complete amorphization was not achieved.

types are clearly distinct, with the zircon-structure-type materials having a higher T_c for the same ENSP ratio. Using T_c as the amorphization criterion, the ENSP ratio can distinguish between the two structure types and clearly gives the correct order within each. Using E_a as the amorphization criterion results in a somewhat worse correlation, especially for the zircon-structure materials, which generally decrease with increasing ENSP, but which show a considerable spread. This is not surprising: as noted above, the E_a values calculated by Eq. (2) can vary substantially as a result of experimental error; whereas, the T_c values do not and, in fact, can be checked experimentally.

Zinkle[11,47] found that the ENSP had to be greater than a certain threshold value (e.g., a value of 10 for $MgAl_2O_4$ or over 1500 for Al_2O_3) before the ionization effects become important. Below these values, no correlation between defect density and the ratio of electronic-to-nuclear energy loss was observed. The ENSP values for the orthophosphates have a narrow range and are even lower than the cutoff values for $MgAl_2O_4$. In the present case, the differences in ENSP ratio are due to target composition and not to the irradiation parameters (e.g., ion type and ion energy). These data, therefore, suggest that the orthophosphates are highly sensitive to the ''annealing effects'' of ionizing radiation, consistent with their ease of crystallization under subthreshold electron irradiation.[23,24]

E. Effect of impurities

Chemical impurities in the natural monazite lower the critical amorphization dose and correspondingly lead to an increase in T_c (Fig. 8). Natural monazite is considerably easier to amorphize at elevated temperatures than pure $LaPO_4$, and it is easier to amorphize than expected based on the stopping powers and cross sections alone. The ''average'' mass of the A-site cation (Table I) is equivalent to that of Nd; hence, Fig. 8 compares the results for natural monazite and $NdPO_4$. Both T_c and E_a are higher for the natural monazite. Perhaps coincidentally, monazite has the lowest value of D_0 (Table II). These observations suggest that the presence of impurities such as Th, Fe, Ca, and Si which, although of acceptable radius, do not have the proper valence (hence charge balance must be maintained by coupled substitution mechanisms[54]) increases the susceptibility to amorphization. Thus, for every Th atom incorporated into the structure, one Si or one Ca atom must also ''crystallize'' to maintain charge balance. The constraints thus produced on the point-defect recombination during the relaxation period after each impact act to lower the value of Δr, the radius of the material that ''recrystallizes'' epitaxially at the edge of each cascade. Alternatively, the increase in T_c may be a result of a decrease in defect mobilities due to trapping at impurities.

V. CONCLUSIONS

The monazite-structure orthophosphates have lower critical temperatures for amorphization than their zircon-structure analogs and are, in general, more difficult to amorphize at elevated temperatures.

Within each crystal structure, the critical amorphization temperature increases with the atomic number of the A-site cation.

Phosphates and silicates with the same crystal structure show large differences in their response to irradiation. The phosphates have lower critical temperatures of amorphization and activation energies for dynamic diffusion-driven irradiation-enhanced epitaxial recrystallization.

The activation energies calculated using the model of Weber *et al.*[34,41] may vary by more than 100% as a result of experimental error and by errors in selecting D_0. T_c values are more reliable indicators of the kinetics of amorphization.

Structural-topology-based models correctly predict the relative susceptibility to amorphization for the monazite and zircon structures in general (with certain assumtpions), but cannot account for the observed differences for compounds *within* each structure type.

The ENSP ratios correlate well with T_c and correctly pre-

dict the amorphization kinetics within each structure. The ENSP ratios also emphasize the differences between these two structures. Electronic energy loss appears to promote defect recombination in these materials for the 800 keV Kr^{2+} irradiations, consistent with previous results for subthreshold electron irradiation.

The effect of chemical impurities in natural samples appears to enhance the resistance to crystallization during irradiation (increasing T_c and E_a). This may be due to restrictions imposed by charge balance or because of defect trapping at impurities during the defect recombination stages of cascade development.

ACKNOWLEDGMENTS

The authors thank the staff at the HVEM-Tandem Facility at Argonne National Laboratory for their assistance with the ion irradiations. We thank L. M. Wang, S. J. Zinkle, and W. J. Weber for important reviews of this manuscript. This work was supported by the Office of Basic Energy Sciences, U.S. DOE (Grant No. DE-FG03-93ER45498). A.M. acknowledges financial support from les Fonds pour la Formation de Chercheurs et de l'Aide á la Recherche (FCAR, Québec). This work was also supported in part by a research grant to A.M. from the Mineralogical Society of America

*Present address: Oak Ridge National Laboratory, Solid State Division, MS 6057, P.O. Box 2008, Oak Ridge, TN.

†Present address: Dept. of NE&RS, University of Michigan, 2355 Bonisteel Blvd., Ann Arbour, MI 48109-2104.

[1] A. Mariano, in *Reviews in Mineralogy*: *Geochemistry and Mineralogy of the Rare Earth Elements*, edited by B. R. Lipin and G. A. McKay (Mineralogical Society of America, Washington, DC, 1989), Vol. 21, pp. 309–334.

[2] Y. Ni, J. M. Hughes, and A. N. Mariano, Am. Mineral. **80**, 21 (1995).

[3] W. O. Milligan, D. F. Mullica, G. W. Beall, and L. A. Boatner, Acta Crystallogr., Sect. C: Cryst. Struct. Commun. **39**, 23 (1983).

[4] W. O. Milligan, D. F. Mullica, G. W. Beall, and L. A. Boatner, Inorg. Chim. Acta **60**, 39 (1982).

[5] F. D. Bloss, *Crystallography and Crystal Chemistry* (Mineralogical Society of America, Washington, DC, 1994), p. 545.

[6] A. T. Aldred, Acta Crystallogr., Sect. B: Struct. Sci. **40**, 569 (1984).

[7] D. F. Mullica, D. A. Grossie, and L. A. Boatner, J. Solid State Chem. **58**, 71 (1985).

[8] D. F. Mullica, W. O. Milligan, D. A. Grossie, G. W. Beall, and L. A. Boatner, Inorg. Chim. Acta **95**, 231 (1984).

[9] L. A. Boatner and B. C. Sales, in *Radioactive Waste Forms For the Future*, edited by W. Lutze and R. C. Ewing (Elsevier, Amsterdam, 1988), pp. 495–564.

[10] I. A. Bondar', I. A. Domanskii, L. P. Mezentseva, M. G. Degen, and L. E. Kalinina, J. Inorg. Chem. **21**, 1126 (1976).

[11] S. J. Zinkle, J. Nucl. Mater. **219**, 113 (1995).

[12] R. Devanathan, N. Yu, K. E. Sickafus, and M. Nastasi, J. Nucl. Mater. **232**, 59 (1996).

[13] L. M. Wang, W. L. Gong, and R. C. Ewing, in *Defect-Interface Interactions*, edited by E. P. Kvam *et al.*, MRS Symposia Proceedings No. 319 (Materials Research Society, Pittsburgh, 1994), p. 247.

[14] R. C. Ewing, W. Lutze, and W. J. Weber, J. Mater. Res. **10**, 243 (1995).

[15] R. C. Ewing, W. J. Weber, and W. Lutze, in *Crystalline Ceramics: Waste Forms for the Disposal of Weapons Plutonium. NATO Workshop Proceedings*, edited by E. R. Merz and C. E. Walter (Academic, Dordrecht, The Netherlands, 1996), pp. 65–83.

[16] B. E. Burakov, E. B. Anderson, V. S. Rovsha, S. V. Ushakov, R. C. Ewing, W. Lutze, and W. J. Weber, in *Scientific Basis for Nuclear Waste Management XIX*, edited by W. M. Murphy and D. A. Knecht (Plenum, New York, 1996), pp. 33–40.

[17] L. A. Boatner, G. W. Beall, M. M. Abraham, C. B. Finch, P. G. Huray, and M. Rappaz, in *Scientific Basis for Nuclear Waste Management*, edited by C. J. M. Northrup, Jr. (Plenum, New York, 1980), Vol. 2, pp. 289–296.

[18] L. A. Boatner, M. M. Abraham, and M. Rappaz, in *Scientific Basis for Nuclear Waste Management*, edited by J. G. Moore (Plenum, New York, 1981), Vol. 3, pp. 181–188.

[19] M. Sasoh, S. Miyamoto, M. Toyohara, and M. Wada (unpublished).

[20] C. W. White, J. D. Budai, J. G. Zhu, S. P. Withrow, R. A. Zuhr, D. M. Hembree, Jr., D. O. Henderson, A. Ueda, Y. S. Tung, R. Mu, and R. H. Magruder, J. Appl. Phys. **79**, 1876 (1996).

[21] C. W. White, J. D. Budai, J. G. Zhu, S. P. Withrow, and M. J. Aziz, Appl. Phys. Lett. **68**, 2389 (1996).

[22] L. Babsail, N. Hamlin, and P. Townsend, Nucl. Instrum. Methods Phys. Res. B **59/60**, 1219 (1991).

[23] A. Meldrum, L. A. Boatner, and R. C. Ewing, J. Mater. Res. **12**, 1816 (1997).

[24] A. Meldrum, L. A. Boatner, and R. C. Ewing, in *Microstructure Evolution during Irradiation*, edited by I. M. Robertson, G. S. Was, L. W. Hobbs, and T. Diaz del la Rubia, MRS Symposia Proceedings No. 439 (Materials Research Society, Pittsburgh, 1997), p. 697.

[25] J. A. Speer, in *Reviews in Mineralogy: Orthosilicates*, edited by P. H. Ribbe (Mineralogical Society of America, Washington, DC, 1982), Vol. 5, pp. 67–112.

[26] L. Heaman and R. R. Parrish, in *MAC Short Course on Radiogenic Isotope Systems*, edited by L. Heaman and J. N. Ludden (Mineralogical Association of Canada, Toronto, 1991), Vol. 19 pp. 59–102.

[27] T. E. Krogh, Geochim. Cosmochim. Acta **46**, 637 (1982).

[28] L. T. Silver, in *Stable Isotope Geochemistry: A Tribute to Samuel Epstein*, edited by H. P. Taylor *et al.* (The Geochemical Society, New York, 1991), Special Publication No. 3, pp. 391–407.

[29] Y. Eyal and D. R. Olander, Geochim. Cosmochim. Acta **54**, 1867 (1990).

[30] D. R. Olander and Y. Eyal, Geochim. Cosmochim. Acta **54**, 1879 (1990).

[31] D. R. Olander and Y. Eyal, Geochim. Cosmochim. Acta **54**, 1889 (1990).

[32] L. M. Wang and R. C. Ewing, Nucl. Instrum. Methods Phys. Res. B **65**, 324 (1992).

[33] W. J. Weber, J. Mater. Res. **5**, 2687 (1990).

[34] W. J. Weber, R. C. Ewing, and L. M. Wang, J. Mater. Res. **9**, 688 (1994).

[35] J. F. Ziegler, TRIM Version 96.01 (IBM-Research, Yorktown, NY, 1996).

[36] M. L. Miller and R. C. Ewing, Ultramicroscopy **48**, 203 (1992).

[37] H. Abe, H. Naramoto, A. Iwase, and C. Kinoshita, Nucl. Instrum. Methods Phys. Res. (to be published).

[38] F. G. Karioris, K. Appaji Gowda, and L. Cartz, Radiat. Eff. Lett. Sect. **58**, 1 (1981).
[39] F. G. Karioris, K. Appaji Gowda, L. Cartz, and J. C. Labbe, J. Nucl. Mater. **108 & 109**, 748 (1982).
[40] M. T. Robinson, Phys. Rev. B **27**, 5347 (1983).
[41] W. J. Weber and L. M. Wang, Nucl. Instrum. Methods Phys. Res. B **91**, 63 (1994).
[42] F. F. Morehead, Jr. and B. L. Crowder, Radiat. Eff. **6**, 27 (1970).
[43] A. Meldrum, L. A. Boatner, L. M. Wang, and R. C. Ewing, Nucl. Instrum. Methods Phys. Res. B **127/128**, 160 (1997).
[44] A. Meldrum, L. M. Wang, and R. C. Ewing, Nucl. Instrum. Methods Phys. Res. B **116**, 220 (1996).
[45] B. C. Sales, R. A. Zuhr, J. C. McCallum, and L. A. Boatner, Phys. Rev. B **46**, 3215 (1992).
[46] S. J. Zinkle, Nucl. Instrum. Methods Phys. Res. B **91**, 234 (1994).
[47] S. J. Zinkle, in *Microstructure Evolution during Irradiation* (Ref. 24), p. 667.
[48] J. S. Im and H. A. Atwater, Appl. Phys. Lett. **57**, 1766 (1990).
[49] G. A. McKay, in *Reviews in Mineralogy: Geochemistry and Mineralogy of the Rare Earth Elements*, edited by B. R. Lipin and G. A. McKay (Mineralogical Society of America, Washington, DC, 1989), Vol. 21, pp. 45–97.
[50] L. W. Hobbs, Nucl. Instrum. Methods Phys. Res. B **91**, 30 (1994).
[51] S. X. Wang, L. A. Wang, and R. C. Ewing, in *Microstructure Evolution during Irradiation* (Ref. 24), p. 619.
[52] L. W. Hobbs, A. N. Sreeram, C. E. Jesurum, and B. A. Berger, Nucl. Instrum. Methods Phys. Res. B **116**, 18 (1996).
[53] J. F. Ziegler, J. P. Biersack, and U. Littmark, *The Stopping and Range of Ions in Solids* (Pergamon, New York, 1985), Vol. 1.
[54] B. Van Emden, M. R. Thornber, J. Graham, and F. J. Lincoln, Can. Min. **35**, 95 (1997).